DEVELOPMENT OF REGIONAL PHASE TOMOGRAPHIC ATTENUATION MODELS FOR EURASIA

Thorne Lay[1], Xiao-Bi Xie[1], and Xiaoning (David) Yang[2]

University of California, Santa Cruz[1] and Los Alamos National Laboratory[2]

Sponsored by National Nuclear Security Administration

Contract No. DE-FC52-05NA26606[1]and DE-AC52-06NA25396[2]
Proposal No. BAA05-23

ABSTRACT

We are developing regional-phase (*Pn*, *Pg*, *Sn*, *Lg*) tomographic attenuation models for Eurasia. The models will be integrated into the National Nuclear Security Administration (NNSA) Knowledge Base and used in the Magnitude and Distance Amplitude Correction (MDAC) station calibration for the development of regional seismic discriminants. Our current focus is on *Pn*, an extremely important phase in seismic event identification.

Accurately accounting for regional-phase geometric spreading is critical for the development of useful attenuation models. It is particularly important for *Pn* and *Sn* waves because the propagation mode of these waves makes them more susceptible to upper mantle velocity structures and the Earth's sphericity, which in turn causes the geometric spreading of *Pn* (and *Sn*) to be dependent on frequency as well as on range in a complicated way. We conduct numerical simulations to quantify *Pn* and *Sn* geometric spreading in a spherical Earth model with constant mantle velocities. Based on our simulation results, we have presented new *Pn* and *Sn* geometric spreading models in the form $G(r, f) = [10^{n_3(f)} / r_0](r_0 / r)^{n_1(f)\log(r_0/r)+n_2(f)}$ and $n_i(f) = n_{i1}\left[\log(f / f_0)\right]^2 + n_{i2}\log(f / f_0) + n_{i3}$, where i = 1, 2, or 3; r is epicentral distance; f is frequency; r_0 = 1 km and f_0 = 1 Hz. We derive values of coefficients n_{ij} by fitting the model to computed *Pn* and *Sn* amplitudes for a spherical Earth model having a 40-km-thick crust, generic values of *P* and *S* velocities and a constant-velocity uppermost mantle.

We applied the new spreading model to observed data in Eurasia to estimate average *Pn* attenuation, obtaining more reasonable results compared to using a standard power-law model. Our new *Pn* and *Sn* geometric-spreading models provide generally applicable reference behavior for spherical Earth models with constant uppermost-mantle velocities.

We have extended numerical modeling of *Pn* behavior in the presence of laterally varying structure in both the Moho discontinuity and fine-scale structure of the uppermost mantle lid. Observations of *Pn* show larger path variance than for other regional phases, and we find that even weak heterogeneities in the lid can produce large scatter in *Pn* amplitudes and significant deviations from the ideal geometric spreading relation shown above. Statistical influences of random heterogeneities are established by many models, and implications for the attenuation inversions are considered.

OBJECTIVE

The objective of this project is to develop 1-Hz, two-dimensional, regional-phase (*Pn, Pg, Sn* and *Lg*) tomographic attenuation models for Eurasia. The models will be used in MDAC for improved event identification.

RESEARCH ACCOMPLISHED

Pn geometric spreading

Accurately accounting for geometric spreading is critical for the development of meaningful regional-phase attenuation models. This is particularly true for *Pn* and *Sn* waves because the nature of their wave propagation renders them acutely sensitive to upper mantle velocity structure and the Earth's sphericity. Even simple one-dimensional (1D) velocity models can produce geometric spreading of *Pn* and *Sn* that is strongly dependent on frequency and range (e.g., Sereno and Given, 1990). If frequency dependence of the geometric spreading actually occurs and is neglected, the attenuation model will acquire incorrect frequency dependence. Similar arrival times of *Pg* and *Pn* phases and *Pn* and *P* phases at their respective crossover distances result in rapidly changing *P*-wave amplitudes, difficulty in phase isolation and identification, and uncertainty in appropriate specification of the propagation path and geometric spreading at these distances. Lateral variation of Moho topography and upper-mantle lid velocity and fine-scale heterogeneity of the lower crust and/or mantle lid further introduce 2D and 3D complexities into *Pn* and *Sn* spreading.

In our previous modeling efforts, primarily based on the reflectivity method and earth flattening transform (EFT) of the spherical model under consideration, we generate complete synthetic seismograms within a specified slowness range for 1D, plane-layered velocity models. The EFT transformations of velocity v and depth z are (Chapman, 1973; Müller, 1977)

$$v_f = \frac{R}{R - z_r} v_r \quad \text{and} \quad z_f = R \ln\left(\frac{R}{R - z_r}\right), \tag{1}$$

where R is the radius of the Earth. Subscript r designates values in the spherical (radially symmetric) model and subscript f designates values in the plane (flat) model. The density ρ transformation is

$$\rho_f = \left(\frac{R}{R - z_r}\right)^m \rho_r, \tag{2}$$

which is not unique since m can take any value between -5 and 1. For regional body-waves, the choice of m is not critical (Müller, 1977). We choose m = -1 for *P*/*SV* simulations (Müller, 1977) and m = -5 for *SH* simulations (Chapman, 1973). We experimented with different values of m, and the results were basically unchanged. Finally, the transformation of amplitudes calculated from plane-model simulations back to corresponding amplitudes in the spherical model is

$$A_r = \left(\frac{\Delta}{\sin\Delta}\right)^{1/2} \left(\frac{R}{R - Z_r}\right)^{\frac{m+5}{2}} A_f, \tag{3}$$

where Z_r is the depth of the source in the spherical model and Δ is epicentral distance in radians.

We approximate the velocity gradient resulting from the EFT (Equations 1 and 2) with homogeneous layers in the plane Earth model, as is required by the reflectivity method. The thickness of these layers affects the accuracy of the approximation, with thinner layers yielding more accurate results. We set the thickness of these layers to be about 0.4 of the minimum wavelength of the waves to be modeled, which appears to be more than adequate. Further reducing the ratio (e.g., from 0.4 to 0.2 of the minimum wavelength) does not alter the results appreciably. The total thickness of the gradient zone is set to be more than 100 km larger than the maximum penetration depth of the direct wave in a homogeneous spherical model recorded at the longest epicentral distance considered. This thickness guarantees that no *Pn* or *Sn* waves observed within the distance range of interest are affected by the lower boundary of the gradient zone. Below the gradient zone, the velocity is constant.

We use the same generic spherical Earth model considered by Sereno and Given (1990) as the Base Earth Model for our simulations and use the synthetics from the simulation to derive parameters of the *Pn* and *Sn* geometric-spreading models that we develop. The Base Earth Model consists of a 40-km-thick outer layer, representative of an average continental crust, with a constant-velocity mantle underneath (Figure 1). The model has no anelastic attenuation. The simplicity of this model allows us to isolate the effects of the sphericity on *Pn* and *Sn* geometric spreading. We use an isotropic point source for *Pn* simulations. The source for *Sn*(*SH*) simulations is a fundamental fault vertical strike-slip source and the source for *Sn*(*SV*) simulations is a dip-slip source. For all source types in our main calculations, a delta function is used as the source time function; source depth is 15 km and source strength is 10^{15} N m. Three-component synthetic ground displacements are computed at 33 locations distributed log-evenly along a linear profile from 200 km (1.8°) to 2,500 km (22.5°). The Nyquist frequency of the seismograms is 20 Hz.

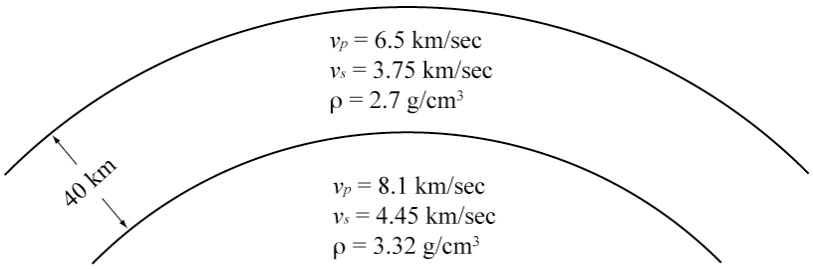

Figure 1. Base Earth model used for *Pn* and *Sn* simulations and the development of new *Pn* and *Sn* geometric-spreading models. Quality factor *Q* is infinite throughout the model.

We cut *Pn* and *Sn* portions of the synthetic seismograms using fixed-velocity windows. The velocities that we use to define the widths of *Pn* windows are 7.6 km/sec and 8.2 km/sec and those for *Sn* windows are 4.0 km/sec and 4.7 km/sec (Hartse, et al., 1997). The windows are centered at the peaks of the phases. We also tested a fixed-window-width method, and the results remained essentially the same. We window *Pn* and *Sn*(*SV*) from vertical-component seismograms and *Sn*(*SH*) from transverse-component seismograms. After *Pn* and *Sn* seismograms are windowed, we taper the seismograms with small tapers (between 2% to 20% depending on the length of the signal relative to the window length) and Fourier transform the seismograms to obtain the amplitude spectra. We make spectral-amplitude measurements at 100 frequencies log-evenly distributed between 0.75 and 13 Hz. Amplitude at each frequency f_i is calculated by taking the average of the amplitudes between frequencies $f_i/\sqrt{2}$ and $\sqrt{2}\, f_i$.

Pn Modeling Results for the Base Earth Model

To visualize the *Pn* amplitude decay in a spherical Earth model, we plot 10-Hz *Pn* amplitudes for the base model in Figure 2. We extend the epicentral-distance range to between 135 km (1.2°) and 8,000 km (71.9°) for this particular simulation in order to better depict the evolution of *Pn* waves. Amplitudes at distances beyond about 20° are measured from the direct wave that has been completely separated from the interference head waves. The amplitudes are corrected for the free-surface effect, which is only important at teleseismic distances. Also plotted in the figure are the amplitude decay of a conical head wave in a plane one-layer-over-half-space model (Aki and Richards, 2002; Eq. 6.26) and the amplitude decay of infinite-frequency direct wave in a spherical Earth model from ray tracing. At distances close to the critical distance, *Pn* geometric spreading behaves like that of a conical head wave. As distance increases, *Pn* spreading starts to deviate from that of the head wave and at about 5°, *Pn* amplitudes begin to increase. Ten-Hz direct-wave energy separates from the rest of the interference head wave at about 10°. It is seen from the figure that this separation is manifested in a change in the smoothness of the *Pn* amplitude variation followed by a reduced rate of amplitude increase. In the range beyond the critical distance and before the direct-wave separation, *Pn* evolves from a wave similar to a conical head wave to the interference head wave, which is a superposition of multiple waves reflected from the Moho. As the epicentral distance approaches teleseismic distances, the direct-wave spreading approaches that of the infinite-frequency wave from ray tracing results, as expected. The direct wave dominates the whole *Pn* wave packet at long distances. We do not see any significant difference between spectral amplitudes obtained by windowing the whole *Pn* wave packet and those obtained by just windowing the direct wave

after its separation from the packet. This is consistent with theoretical predictions (Červený and Ravindra, 1971).

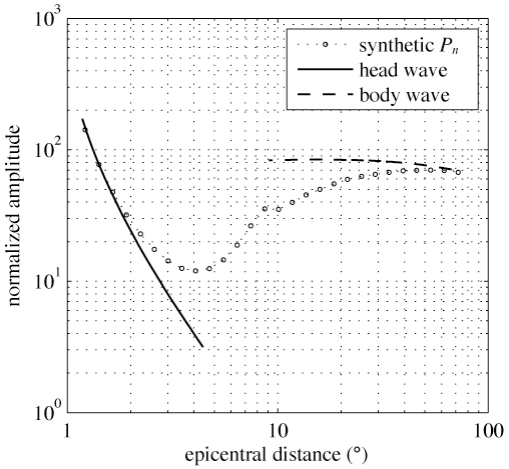

Figure 2. 10-Hz synthetic *Pn* amplitude decay in a spherical Earth model with constant mantle velocities. The solid line depicts the theoretical amplitude decay of a conical head wave in a plane one-layer-over-half-space Earth model. The dashed line is the amplitude decay of infinite-frequency direct wave in a spherical homogeneous Earth model from ray-tracing calculations.

Pn geometric spreading in a spherical Earth model is not only different from that of a head wave as is shown in Figure 2, but also frequency dependent. Figure 3 shows the *Pn* amplitude-variation surface as a function of distance and frequency for the base model. The strong frequency dependence of the amplitudes is apparent. Amplitudes at higher frequencies are affected more by the sphericity than are lower-frequency amplitudes.

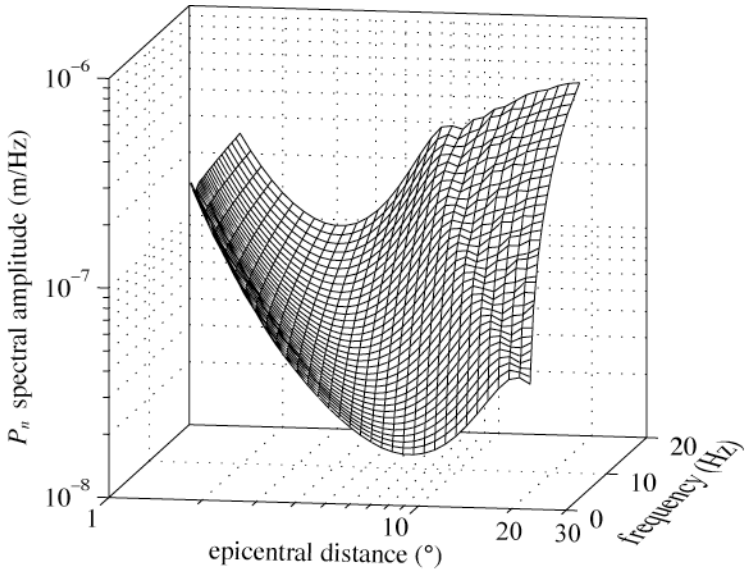

Figure 3. Synthetic *Pn* amplitudes as a function of epicentral distance and frequency.

In last year's report, and as published in Yang et al. (2007) we presented a parameterized description of *Pn* geometric spreading for this simple reference model. The amplitude spectrum of *Pn* can be parameterized as:

$$A(r,\theta,f) = K(f)M_0R(\theta)G(r,f)\exp\left(-\frac{\pi f}{Q(f)v}r\right)S(f) \tag{4}$$

with the new geometric-spreading model expressed as

$$G(r,f) = \frac{10^{n_3(f)}}{r_0}\left(\frac{r_0}{r}\right)^{n_1(f)\log\left(\frac{r_0}{r}\right)+n_2(f)} \qquad (r_0 = 1 \text{ km}) \tag{5}$$

and

$$n_i(f) = n_{i1}\left[\log\left(\frac{f}{f_0}\right)\right]^2 + n_{i2}\log\left(\frac{f}{f_0}\right) + n_{i3} \qquad (i = 1, 2, 3;\ f_0 = 1 \text{ Hz}). \tag{6}$$

In Equation 4, K is a frequency-dependent scaling factor; M_0 is source moment; R is source radiation pattern; Q is *Pn* quality factor; v is *Pn* velocity; S is receiver site response; r is epicentral distance; θ is azimuth angle and f is frequency. r_0 and f_0 are included in Equations 5 and 6 in order for the new model to have the same dimension as standard power-law models (e.g., Sereno et al., 1988). The main differences between the new geometric-spreading model (Equations 5 and 6) and the standard frequency-independent power-law model are the addition of the first term in the exponent and the frequency dependence of parameters n_i. In the logarithm domain, the new model is a quadratic function of log-distance, whereas the power-law model is linear. The reason for choosing a log-quadratic function is to keep the parameterization as simple as possible while providing a good fit to the synthetics. The adoption of a quadratic functional form for n_i (Equation 6) is based on the behavior of n_i versus the frequency obtained by fitting Equation 6 to synthetic *Pn* amplitudes at individual frequencies.

If we take common logarithm of Equation 5, substitute Equation 6 into the result and let r_0 and f_0 equal one, we obtain

$$\begin{aligned}\log[G(r,f)] = {} & n_{11}(\log f)^2(\log r)^2 + n_{12}\log f(\log r)^2 + n_{13}(\log r)^2 \\ & -n_{21}(\log f)^2\log r - n_{22}\log f\log r - n_{23}\log r \\ & +n_{31}(\log f)^2 + n_{32}\log f + n_{33}\end{aligned}, \tag{7}$$

where r is in kilometers and f is in hertz. To derive coefficients n_{ij}, we fit Equation 7 to synthetic *Pn* amplitudes shown in Figure 3 in a least-squares sense. *Pn* amplitudes are corrected for M_0 used in the simulation (10^{15} N m) and K before the fitting. This yielded the coefficients in Table 1.

Table 1 Coefficients of the new *Pn* geometric-spreading model

n_{11}	n_{12}	n_{13}	n_{21}	n_{22}	n_{23}	n_{31}	n_{32}	n_{33}
-0.217	1.79	3.16	-1.94	8.43	18.6	-3.39	9.94	20.7

Similar processing provided an *Sn* geometric spreading model for the Base Earth Model structure.

Pn Spreading Sensitivity to Mantle Velocity Gradients

The velocity structure of the mantle lid is seldom well-constrained. The most direct constraint is provided by the shape of the *Pn* travel time curve as a function of distance over a wide-enough distance range for reliable measurement, and even when there is an apparent travel time branch curvature, it is difficult to distinguish between a smooth gradient with depth versus constant velocity layering with small step increases. Receiver function methods and surface wave dispersion inversions sometimes indicate gradients in the lid structure, but resolution tends to be poor, especially for *P*-velocity. As a result, reference velocity structures often assume constant or near-constant velocity in the mantle lid by default, so our Base Earth Model is not a bad starting point in many cases. However, there are regions where the lid velocity appears to increase or decrease with depth. The effects of positive *P*-velocity gradients in the mantle lid on the frequency-dependent spreading of *Pn* are illustrated in Figure 4. The basic shape of the spreading behavior is preserved, but the distance-behavior shifts systematically to shorter distances, with overall higher *Pn* amplitudes as the gradient increases. It is possible to determine appropriate coefficients for a spreading representation like Equation (7) for any specific gradient, but this is only warranted if there are a priori constraints on the specific model in the region for which the spreading is to be utilized. Of course, the use of an inappropriate spreading relationship will directly map into any inferred frequency-dependent

attenuation structure, so it is clear that precise knowledge of the lid gradient is essential for robust attenuation estimation. This non-linear sensitivity of the spreading to the velocity model is a formidable issue for *Pn* and *Sn* attenuation determination that has not been widely appreciated.

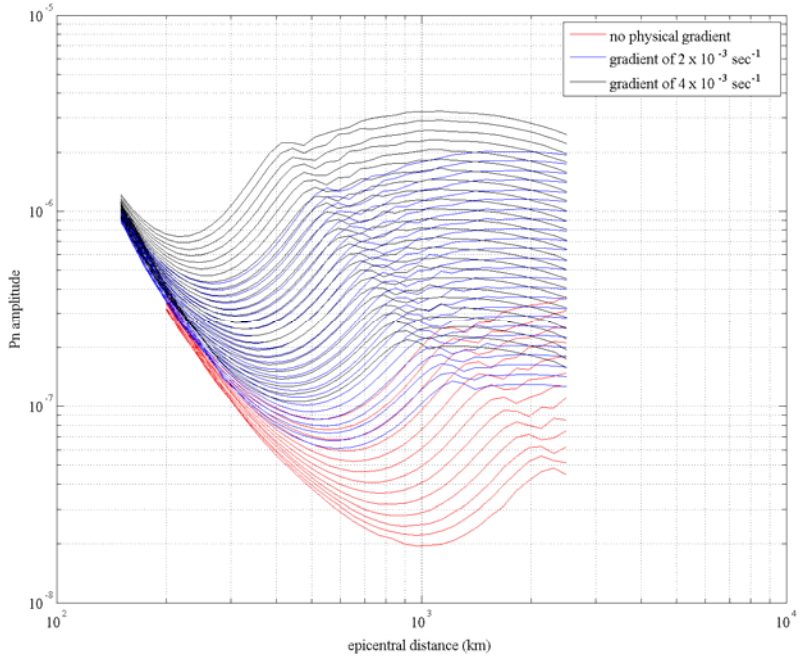

Figure 4. *Pn* amplitude versus distance curves similar to Figure 3, but for the Base Earth Model (red curves, for no physical gradient in the lid) and for two models with mild positive gradients in the mantle lid. The suite of curves for each case corresponds to frequencies ranging from 0.75 Hz (lowest curve) to 12 Hz (highest curve).

Pn Spreading Sensitivity to Lateral Mantle Velocity Heterogeneity

Given the disconcerting sensitivity of *Pn* spreading to a typically poorly-constrained attribute of the reference velocity model (the velocity gradient in the uppermost mantle lid), the prospect of robust attenuation determination for the uppermost mantle appears limited. Most standard seismological practices assume rather simple reference models, known to be gross approximations of the real structure, under the assumption that errors in the reference model produce only mild biases in other properties such as attenuation. This is simply not the case here, given the non-linear sensitivity of the *Pn* and *Sn* whispering gallery arrivals for 1D structures. But the non-linearity itself raises the following question: how stable is the precise behavior in the presence of lateral heterogeneity? Clearly the actual mantle lid has multi-scale lateral heterogeneities; does their presence weaken the acute sensitivity of *Pn* spreading to the reference structure?

We explored the effects of lateral heterogeneity in the mantle lid velocity structure using a 2D finite-difference code (Xie and Lay, 1994) in which we impose random lateral velocity fluctuations characterized by rms velocity fluctuations of a particular strength and horizontal and vertical averaging functions with different length scales. This allows us to consider 2D random heterogeneity models like that shown in Figure 5.

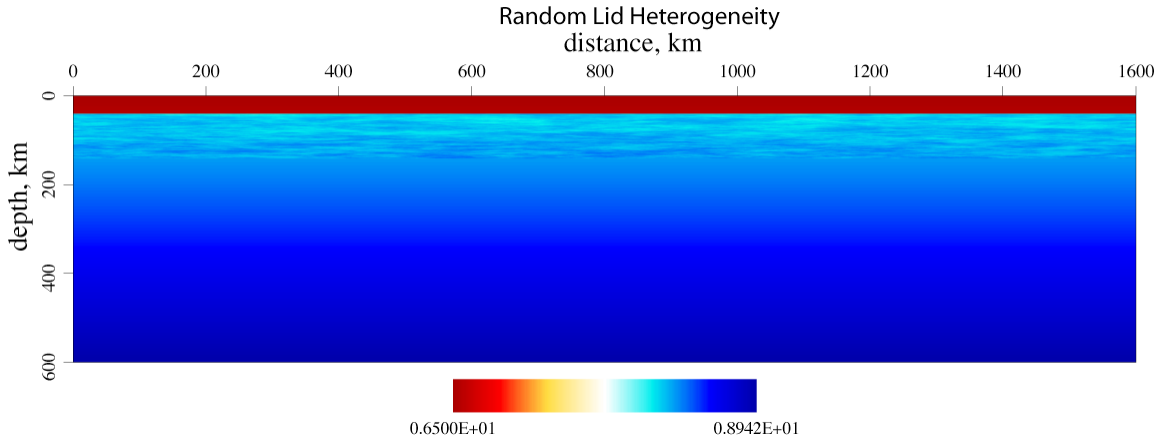

Figure 5. Visualization of the 2D velocity model with 0.5% (rms) *P*-velocity heterogeneity in the upper 100 kilometers of the mantle lid. The background model is the EFT version of the Base Earth Model, so there is a slight positive velocity gradient across the crust and mantle.

The 2D finite-different modeling approach cannot achieve the very high frequencies of the 1D wave-number integration method, as the synthetics are limited to about 1 sec dominant period. Tests with simple 1D models indicate that the basic behavior of *Pn* spreading is accurately reproduced, as shown in Figure 6.

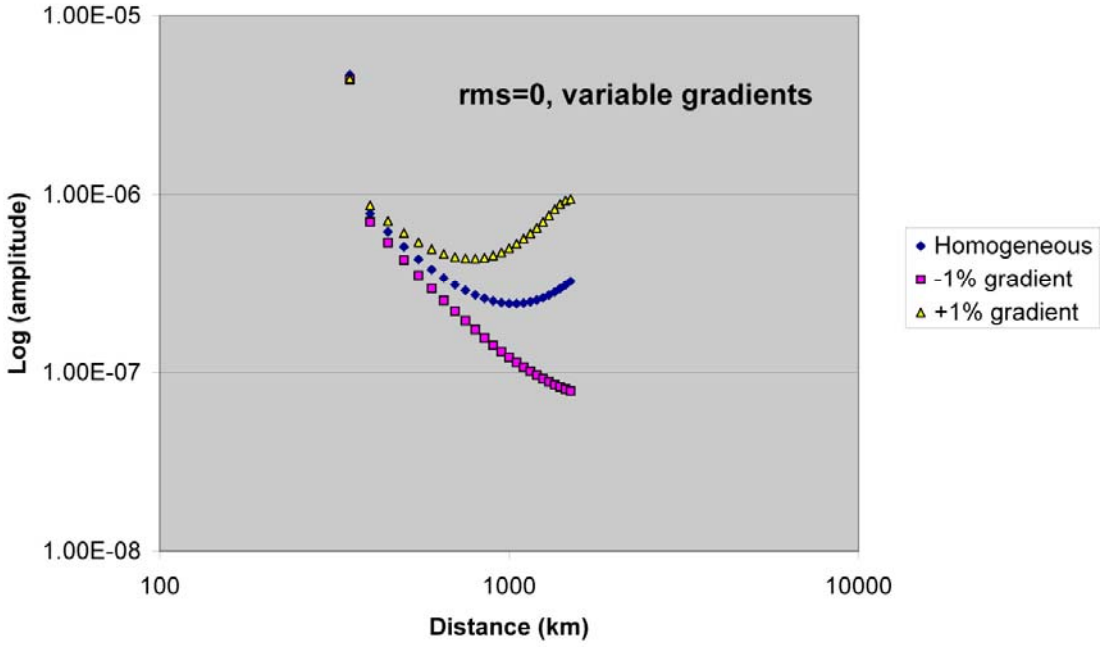

Figure 6. *Pn* amplitude versus distance for the 1D Base Earth Model (Homogeneous) and for models with negative and positive gradients, from synthetics computed by the 2D finite difference method. The dominant period is about 1 sec. The amplitudes are corrected to 3D spreading, but not for the $(\Delta/\sin(\Delta))^{1/2}$ conversion to spherical spreading.

Analysis of effects of random heterogeneity requires a statistical sampling of the effects associated with different realizations of the random-velocity parameters. Many models have been run for various statistical properties of the mantle lid structure, with complete synthetic seismograms being computed.

Figure 7 shows the synthetic *Pn* amplitudes for five realizations of a heterogenous structure with 0.5% rms P-velocity fluctuations with anisotropic averaging lengths of 40 km horizontally and 3 km vertically, along with an average of the ensemble, which can be directly compared to the result for the Base Earth Model.

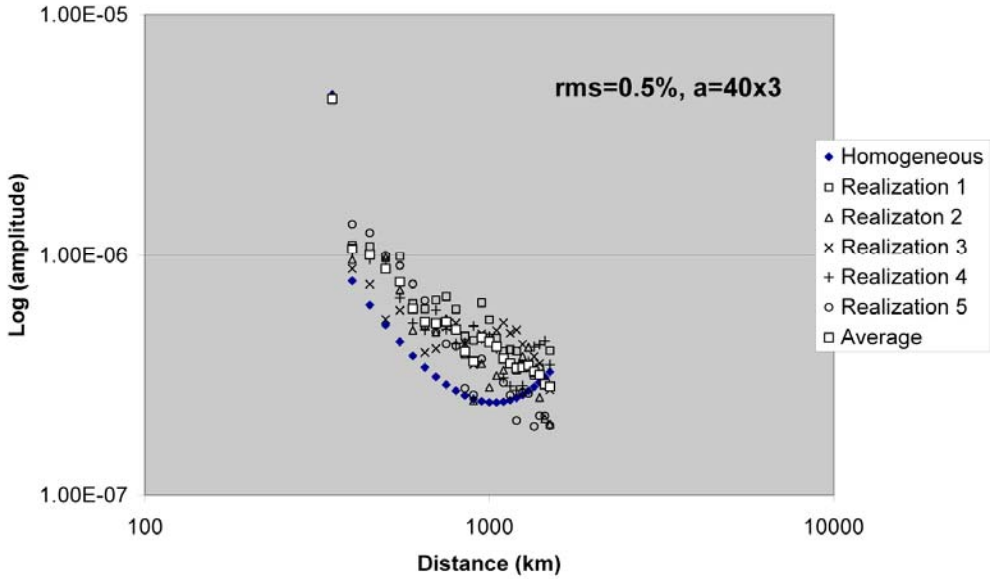

Figure 7. *Pn* amplitudes for five realizations of random velocity models with 0.5% velocity heterogeneity, 40 km horizontal averaging length and 3 km vertical averaging length. The average amplitude (white boxes) can be compared with results for the Base Earth Model.

An interesting behavior in Figure 7 is that the presence of velocity fluctuations affects the basic shape of the spreading, and can be represented well by a power-law type behavior at this frequency. This suggests that the 1D spreading behavior is rather delicate, with modest heterogeneity disrupting the specific interference that gives rise to the complex shape. Similar ensembles of simulations for variable aspect ratios, from isotropic heterogeneities to horizontally elongated heterogeneities (Figure 8), show that the change in spreading from the Base Earth Model to something closer to a power-law behavior increases with the degree of anisotropy (i.e., the minimum in the spreading curve is progressively eliminated as the heterogeneities become more pancake-like). For a specific heterogeneity aspect ratio (40 km x 3 km), the effect of variable rms velocity level is shown in Figure 9. As the strength of the velocity functions increases, there is progressive reduction of curvature of the amplitude-distance trend, and the overall amplitude behavior is increasingly power-law like.

These results present something of a conundrum; the simple 1D velocity structures are very simple, but produce complex geometric spreading behavior that is non-linearly sensitive to the model parameters, while 2D models with geologically realistic lateral heterogeneities produce relatively simple geometric spreading behavior. It is likely that 3D effects will further enhance the tendencies manifested in the 2D calculations. In essence, prior efforts that have assumed simple power-law geometric spreading behavior, which is not a realistic form of spreading for any known 1D velocity model, may actually be reasonable results to the extent that the specific power law corresponds to a viable level of uppermost mantle velocity heterogeneity. Of course, the precise spectrum and statistical distribution of real mantle lid heterogeneities is not known for any specific path, just as the precise 'best' 1D lid velocity gradient is not known. Thus, propagating uncertainties in the geometric spreading model into uncertainties in attenuation model estimates remains very difficult. The effects of the heterogeneities on shorter period signals have not been assessed, and doing so presents formidable computational challenges for long-range *Pn* and *Sn*: the overall frequency-dependent behavior remains to be characterized. The effects of rough Moho structure and deep crustal heterogeneity also need to be evaluated before settling on a procedure for attenuation estimation.

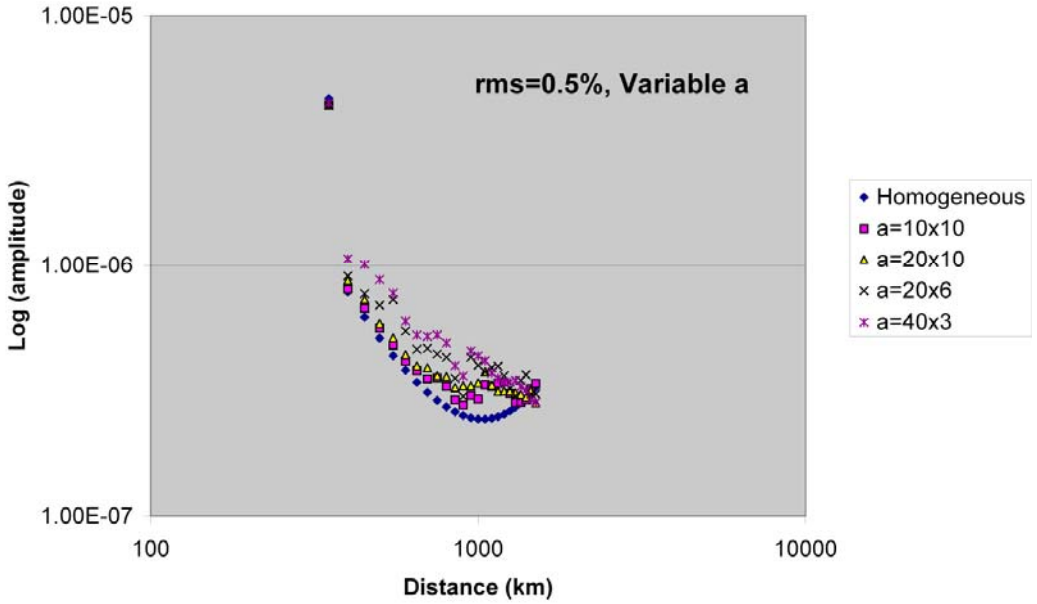

Figure 8. *Pn* amplitudes for averages of ensembles of five realizations for random velocity models with 0.5% rms velocity heterogeneity, with 10 to 40 km horizontal averaging lengths and 10 to 3 km vertical averaging lengths.

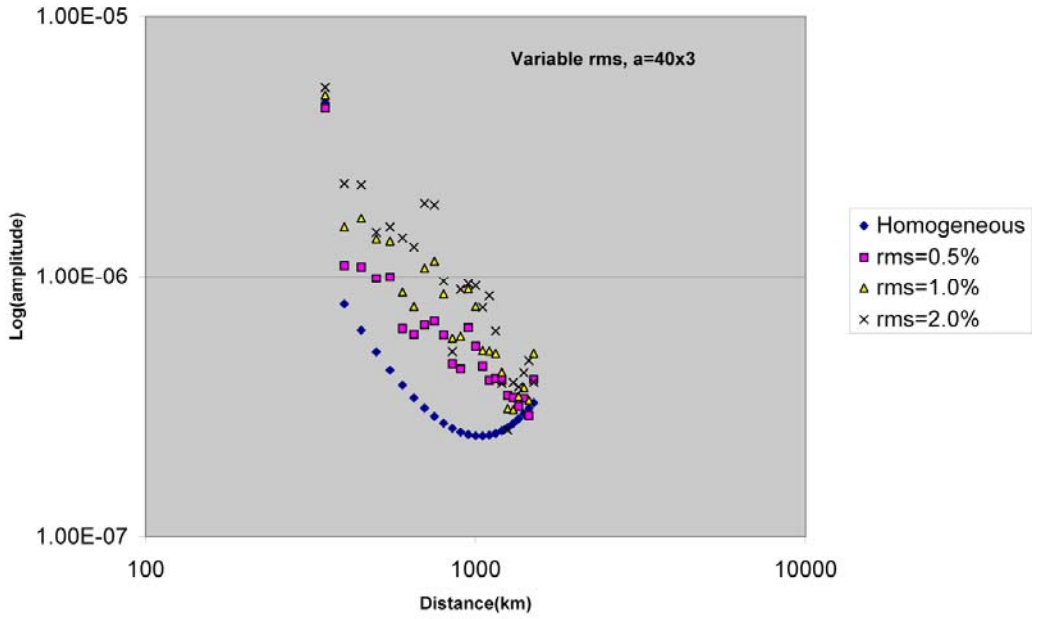

Figure 9. *Pn* amplitudes for averages of ensembles of five realizations for random velocity models with varying 0.5 to 2.0% rms velocity heterogeneity, with 40 km horizontal averaging length and 3-km vertical averaging length.

CONCLUSIONS AND RECOMMENDATIONS

The behavior of geometric-spreading for *Pn* and *Sn* is surprisingly subtle and complex, even for simple 1D reference models (e.g., Menke and Richards, 1980; Sereno and Given, 1990). As anticipated in our report last year, the effects of variable 1D mantle lid gradients have been shown to preserve the basic function form of the frequency-dependent complexity of the constant-velocity mantle lid model, but the effects are so strong that new coefficients would need to be determined for the spreading model to be adequate. Indeed, the sensitivity to gradient is non-linear, raising questions about the choice of spreading model given typical situations where there is little or no information on the local lid velocity gradients. Of course, if the data for a given region are sufficient to constrain the lid velocity gradient (this may be the case across the Russian platform, for example), specific spreading computations can clearly provide a reference behavior relative to which attenuation estimates can be performed. In detail, even this is not going to be easy, given the degenerate nature of layered versus gradient model fits to first arrival times.

Computations with lateral heterogeneities in the mantle lid add an additional, possibly mitigating complexity to the problem of *Pn* and *Sn* geometric spreading. 2D finite-difference simulations indicate that the precise shape of the geometric spreading behavior for 1D models is quickly disrupted by even moderate levels of lateral heterogeneity, and the behavior for 1-sec period waves moves toward a power-law representation as the level of heterogeneity increases and as the horizontal/vertical aspect ratio of the heterogeneities increases. This behavior needs further quantification and exploration of its frequency dependence, but may provide a basis for using a conventional power-law-type geometric spreading with new recognition that the associated model for which it is approximating the amplitude decay is not a conventional 1D constant velocity mantle model or even a constant lid-gradient model, but is intrinsically a statistically heterogeneous model with some form of power-law heterogeneity, akin to those for very complex, multiple-arrival phases such as *Lg*. While specifying the preferred power law is still going to be difficult given the very limited knowledge of actual lid heterogeneity on any given path or in any given region, some understanding of trade-offs with attenuation model inferences may prove possible. Further modeling with rough Moho, crustal heterogeneity, and broader band seismograms is required before final recommendations and attenuation models can be achieved.

REFERENCES

Aki, K., and P. G. Richards (2002). *Quantitative Seismology*, 2nd edition, University Science Books, Sausalito, California.

Červený, V., and R. Ravindra (1971). *Theory of Seismic Head Waves*, University of Toronto Press, Toronto.

Chapman, C. H. (1973). The Earth flattening transformation in body wave theory, *Geophys. J. R. astr. Soc.* 35: 55–70.

Hartse, H. E., S. R. Taylor, W. S. Phillips, and G. E. Randall (1997). A preliminary study of regional seismic discrimination in central Asia with emphasis on western China, *Bull. Seism. Soc. Am.* 87: 551–568.

Menke, W. H., and P. G. Richards (1980). Crust-mantle whispering gallery phases: a deterministic model of teleseismic *Pn* wave propagation, *J. Geophys. Res.* 85: 5416–5422.

Müller, G. (1977). Earth-flattening approximation for body waves derived from geometric ray theory—improvements, corrections and range of applicability, *J. Geophys.* 42: 429–436.

Sereno, T. J., and J. W. Given (1990). *Pn* attenuation for a spherically symmetric Earth model, *Geophys. Res. Lett.* 17: 1141–1144.

Sereno, T. J., S. R. Bratt, and T. C. Bache (1988). Simultaneous inversion of regional wave spectra for attenuation and seismic moment in Scandinavia, *J. Geophys. Res.* 93: 2019–2035.

Xie, X.-B., and T. Lay (1994). The excitation of *Lg* waves by explosions: A finite-difference investigation, *Bull. Seism. Soc. Am.* 84: 324–342.

Yang, X., T. Lay, X.-B. Xie, and M. S. Thorne (2007). Geometric spreading of *Pn* and *Sn* in a spherical Earth model, *Bull. Seism. Soc. Am.* 97: 2053–2065, doi:10.1785/0120070031.